



Research Article

Graphene on Rh(111): A template for growing ordered arrays of metal nanoparticles with different periodicities



Mariano D. Jiménez-Sánchez ^{a, *}, Carlos Romero-Muñiz ^{b, c, **}, Pablo Pou ^{b, d}, Rubén Pérez ^{b, d}, José M. Gómez-Rodríguez ^{a, d, e, 1}

^a Departamento de Física de La Materia Condensada, Universidad Autónoma de Madrid, E-28049, Madrid, Spain

^b Departamento de Física Teórica de La Materia Condensada, Universidad Autónoma de Madrid, E-28049, Madrid, Spain

^c Department of Physical, Chemical and Natural Systems, Universidad Pablo de Olavide, Ctra. Utrera Km. 1, E-41013, Seville, Spain

^d Condensed Matter Physics Center (IFIMAC), Universidad Autónoma de Madrid, E-28049, Madrid, Spain

^e Instituto Nicolás Cabrera, Universidad Autónoma de Madrid, E-28049, Madrid, Spain

ARTICLE INFO

Article history:

Received 20 July 2020

Received in revised form

15 November 2020

Accepted 29 November 2020

Available online 2 December 2020

Keywords:

Nanoparticle arrays

Periodic nanotemplates

2D materials

Graphene

Ir

Rh

Clusters

Density functional theory

ABSTRACT

The development of approaches to provide ordered networks of metal nanoparticles is a topic of great interest due to its potential contribution to the advent of a more efficient technology. The template-assisted formation of ordered nanoparticle arrays on graphene- or h-BN-metal surfaces has profiled as a promising approach because of the periodic interfacial modulations associated to the moiré patterns. Nevertheless, a complete understanding of the requirements that a moiré must meet to act as a good template is still challenging. In order to shed light on this issue, here, the graphene/Rh(111) surface is investigated as model template for the growth of metal nanoparticles due to its large variety of moiré patterns. Scanning tunneling microscopy experiments have revealed different Ir nanoparticle spatial distributions depending on the underlying moiré periodicity ranging from randomly scattered nanoparticles to well-ordered lattices with multiple periodicities. To unveil the origin of this behavior, density functional theory calculations have been performed on representative moiré patterns for the adsorption of both Ir individual adatoms and nanoparticles. We conclude that the presence of distinctive chemical environments throughout the moiré, which controls the size and the adsorption configuration of the nanoparticles, is crucial for the formation of ordered arrays.

© 2020 Elsevier Ltd. All rights reserved.

1. Introduction

Metal nanoparticles have become key elements in the current technology, being present in an important part of today's available products [1,2]. The reduced dimensionality of these elements confers them unique properties. To mention some examples, they have proven to exhibit size dependent electronic structures, characterized by standing electron waves with discrete energy levels that emerge below a certain nanoparticle critical size [3], and optical properties as a localized surface plasmon resonance [3,4]. Moreover, their high surface/volume ratio gives rise to a superior

catalytic activity [5] for chemical reactions of great interest in industry. To further boost the potential of these zero-dimensional elements, huge efforts are being devoted to develop methodologies for producing ordered arrays of metal nanoparticles with the highest possible structural perfection [6–10].

The emergence of nanotechnology as a top priority research field, and its subsequent establishment as one of the strongest pillars supporting the development of new products and services, fostered the design of different approaches to obtain nanoparticles with well-defined shapes and narrow size distributions [11]. The most widespread one consists in the synthesis in solution as colloidal nanoparticles [11,12]. Indeed, most of the advances related to nanoparticles have been achieved so far by using colloidal dispersions [11,12]. These nanoparticles can be subsequently arranged into periodic networks following different approaches [7,8]. Other techniques as the deposition of preformed nanoparticles on graphene supports are also being employed [13,14]. However, in spite of the significant improvements experimented in the above

* Corresponding author.

** Corresponding author. Department of Physical, Chemical and Natural Systems, Universidad Pablo de Olavide, Ctra. Utrera Km. 1, E-41013, Seville, Spain.

E-mail addresses: marianodjimenez@uam.es (M.D. Jiménez-Sánchez), crommun@upo.es (C. Romero-Muñiz).

¹ Deceased 1st, November 2020, Spain.

mentioned methods, a better control in the shape, size and spatial distributions of nanoparticles is still needed. This is an urgent task to be achieved in the near future, in order to satisfy the requirements of an increasingly demanding society.

The growth of metal nanoparticle lattices on periodic templates comprising a 2D layered material of low reactivity and a metal support has been suggested as a promising candidate to overcome the current existing limitations. Specially, those related to the control in the size distribution, as well as in the crystalline quality of the individual units and of the whole network. In particular, metal supported graphene and h-BN monolayers, which are extremely popular 2D materials, whose properties can be tuned by following a large variety of routes [15–26], have proven to be excellent templates [6,27–34]. Investigations of ordered lattices on such interfaces have been mainly performed on Ru(0001) and Ir(111) substrates and are focused on a particular moiré pattern. However, in order to fully exploit the excellent properties of graphene- and h-BN-metal based nanotemplates, further work is still necessary. This includes a better understanding of the role played in the nanoparticle lattices formation by the different periodicities appearing in these systems, which offer distinct bonding landscapes for the adsorption of the atomic aggregates [35].

Graphene monolayers epitaxially grown on Rh(111) surfaces are ideal systems to extract information of general validity on that issue. They are composed of grains whose graphene lattice is unambiguously oriented with respect to the one of the metal substrate underneath, displaying a great variety of possible rotational domains [36]. Each of them is characterized by a different moiré pattern with a given periodicity, offering a distinct interfacial bonding chemistry. Furthermore, the strong interaction with the metal surface induces a spatial modulated chemical reactivity to the originally inert graphene layer [37–40].

In this work, by combining scanning tunneling microscopy (STM) experiments with density functional theory (DFT) calculations the influence of the moiré patterns of graphene on Rh(111) surfaces on the ordering of Ir nanoparticles has been investigated. Different spatial nanoparticle distributions have been found ranging from randomly scattered nanoparticles to well-ordered lattices with different periodicities. By means of STM nanomanipulation the underlying moiré pattern to each nanoparticle spatial distribution has been unveiled, finding out which moiré patterns support the growth of ordered lattices. The graphene/Rh(111) (hereinafter G/Rh(111)) surface has been found the first one to our best knowledge, among all the graphene- or h-BN-metal interfaces reported to date, which allows the formation of multiple nanoparticle superlattices exhibiting different periodicities. DFT calculations performed on representative moiré patterns demonstrate that nanoparticle superlattices formation is ruled by a subtle interplay between the presence of remarkable differences between the chemical environments of the C atoms within the moiré unit cell. The graphene-metal interaction plays a relevant role in the creation of the required atomic bonds necessary for the nanoparticle growth.

The obtained results shed light on the key factors for the growing of ordered nanoparticle superlattices on G/Rh(111) surfaces. Such findings could allow understanding the role played by different moiré patterns in other graphene or h-BN/metal interfaces in the growth of ordered metallic nanoparticles. This could imply a significantly advance in the future development of a systematic route to obtain nanotemplates with different periodicities. On the other hand, the singular presence of multiple superlattice periodicities, together with other spatial distributions, could offer a useful benchmark at atomic scale for future investigations on metallic nanoparticle properties. For instance, the influence on the nanoparticle stability of the size effects [41] could be explored,

which is relevant for the design of future nanocatalysts or nanodots. In fact, G/Rh(111) could even be directly used as a support for Ir-nanoparticle-based catalysis [42,43]. Furthermore, these different superlattice periodicities are remarkable since electrons in the above mentioned quantized levels [3], arising from their quantum confinement in metal nanoclusters, could jump between neighbor aggregates. Therefore, it would be possible to tune that electron transfer using moiré patterns of different periodicities, giving rise to nanoparticle superlattices with different spacing between atomic aggregates.

2. Experimental and theoretical methods

2.1. Experimental methods

Experiments were performed in an ultrahigh vacuum (UHV) system. It consists of two chambers with independent pumping: one for sample preparation and the other for their characterization at the atomic scale by means of a home built variable temperature scanning tunneling microscope (VT-STM) [44]. Rh(111) surfaces were prepared by a cycling procedure of Ar⁺ sputtering at 1 keV and subsequent annealing to 1200 K at an oxygen partial pressure of 2×10^{-7} Torr. At the end of each cycle, the sample was flash annealed at 1300 K during 60 s without supplying O₂ into the chamber.

Graphene monolayers were obtained by chemical vapor deposition (CVD-UHV), in the same UHV chamber employed for the preparation of the Rh(111) substrate, by using ethylene (C₂H₄) as a precursor. Specifically, the metal substrate was kept at 1120 K, while it was exposed to an ethylene partial pressure of 3×10^{-7} Torr during 180 s.

Ir deposition was carried out from a homemade evaporator consisting on a current heated wire of that material. The sample was kept at room temperature during the deposition. Typical deposition rates of 0.1 ML/min were employed. Coverages were calibrated after Ir deposition on bare Ir(111) surfaces by means of STM.

STM data acquisition was carried out at RT, by using electrochemically etched W tips, in the constant current mode, with the bias voltage applied to the sample. Data acquisition and processing were performed by using the WSxM software [45].

2.2. Theoretical methods

The theoretical approach was based on DFT calculations. Plane-wave calculations were performed using the VASP package [46] with a cutoff of 400 eV for the basis set and pseudopotentials constructed with the projected augmented wave method [47,48]. The PBE functional (Perdew-Burke-Ernzerhof) [49] was chosen for the description of electronic exchange and correlation, supplemented by the Grimme's D2 semi-empirical correction [50] to account for the dispersion interactions.

Two unit cells corresponding to different hexagonal moiré patterns found in the G/Rh(111) interface have been considered: The RDO_{11×11} moiré with a size of 29.7 Å, which comprises a total of 774 atoms and the RDO_{6×6} moiré, with a periodicity of 16.2 Å and 230 atoms. In both cases, the cells contain a four-layer slab of rhodium in which the graphene layer has been adsorbed on top. All structures were fully relaxed following a conjugate gradient algorithm until forces upon atoms were smaller than 0.01 eV Å⁻¹. During the optimization, the two deepest layers of the slab were frozen in their bulk positions while the rest of the atoms were allowed to relax. The reciprocal space was sampled only in the Γ -point in the larger cell and with a $2 \times 2 \times 1$ Monkhorst-Pack grid [51] in the smaller cell.

The adsorption and diffusion process of single Ir atoms were studied by placing one Ir atom on different regions of the moiré pattern and allowing the subsequent relaxation. The adsorption energy of Ir adsorbates is calculated as usual: $E_{\text{ad}} = E[\text{Ir}/\text{G}/\text{Rh}(111)] - E[\text{G}/\text{Rh}(111)] - E[\text{Ir}]$, where $E[\text{Ir}/\text{G}/\text{Rh}(111)]$ is the energy of the whole system while $E[\text{G}/\text{Rh}(111)]$ and $E[\text{Ir}]$ are the energies of the moiré pattern and the isolated Ir atom respectively. The Climbing Image Nudged Elastic Band (CI-NEB) method [52] has been used to find minimum-energy paths for the diffusion of single Ir atoms on the G/Rh(111) surface. In these calculations the convergence criterion in forces was lowered to $0.05 \text{ eV } \text{Å}^{-1}$ while a spring constant of $1.5 \text{ eV } \text{Å}^{-2}$ was employed between the three intermediate images considered during the calculations. In addition, planar clusters of 7 and 19 Ir atoms adsorbed in several locations of the unit cell were studied for both moiré structures. These clusters were constructed following a (111) arrangement and the same relaxation criteria were used to obtain their equilibrium geometries.

3. Results and discussion

Fig. 1a shows a large scale STM topography acquired after room temperature (RT) deposition of $0.50 \pm 0.05 \text{ ML}$ Ir on a graphene monolayer epitaxially grown on a Rh(111) substrate. As observed, size and spatial distributions of the resulting nanoparticles are rather inhomogeneous all over the G/Rh(111) surface. While, at the upper left part of the topography, the resulting atomic aggregates are randomly distributed over the surface, at the lower right part, they are much smaller and are arranged into a hexagonally symmetric superlattice. These differences in the spatial distribution of nanoparticles can be observed in the Fast Fourier Transform obtained in a zoomed-in portion of the respective regions (see the insets).

The question of why the size and spatial distributions of the nanoparticles are so inhomogeneous along this particular graphene surface becomes unavoidable. To provide an answer to this question, nanoparticles were removed from a number of regions in different samples to analyze the portion of the G/Rh(111) surface on

which they were adsorbed. Nanoparticle removal was carried out by using the STM tip (see Fig. 1b) following the procedure reported in Ref. [32]. Specifically, the piezo scan was stopped and the tip was placed over the position of the nanoparticle that is intended to be removed. Afterwards, the feedback loop was opened and, subsequently, the tip was approached towards the nanoparticle by typical distances of $0.5\text{--}0.7 \text{ nm}$. Then, the tip was moved back away from the sample and the feedback loop was connected again. As a result, the nanoparticle is removed, leaving behind a cluster vacancy in the superlattice. To demonstrate the performance of this methodology, Fig. 1c–d shows two STM topographies acquired in the same sample area before and after the removal of the nanoparticle encircled in Fig. 1c by a black circumference.

By systematically repeating the above mentioned procedure, it was possible to remove nanoparticles from a number of areas belonging to different samples to uncover the region of the G/Rh(111) surface, on which they were sitting on. As an example, Fig. 1e shows a region around a boundary between an area, where nanoparticles are arranged into a periodic lattice, and another one, where they do not exhibit any apparent ordering. Fig. 1f shows a STM image acquired in the same area as visualized in Fig. 1e after the removal of almost all the nanoparticles. A boundary between graphene flakes exhibiting different moiré patterns can be clearly observed in Fig. 1f. Notice that the upper right part of this image shows the most common moiré pattern found in G/Rh(111) surface. This pattern is formed in the rotational domain for which the relative angle between graphene and Rh(111) lattices is 0° , and a (11×11) supercell, as referred to the Rh(111) substrate, matches with a (12×12) one of the graphene lattice [36,53]. Then, on the following it will be denoted as $\text{RDO}_{11 \times 11}$. Here, it is convenient to mention that the identification of the rotational domains, associated to the different moiré patterns shown along this work, has been performed by following the procedure reported in Ref. [36]. Thus, according to that approach, the moiré pattern, observed at the lower left part of Fig. 1f has been ascribed to the rotational domain for which the graphene lattice is rotated by 3.6° degrees with respect to that of the Rh(111) surface underneath. As a result, a

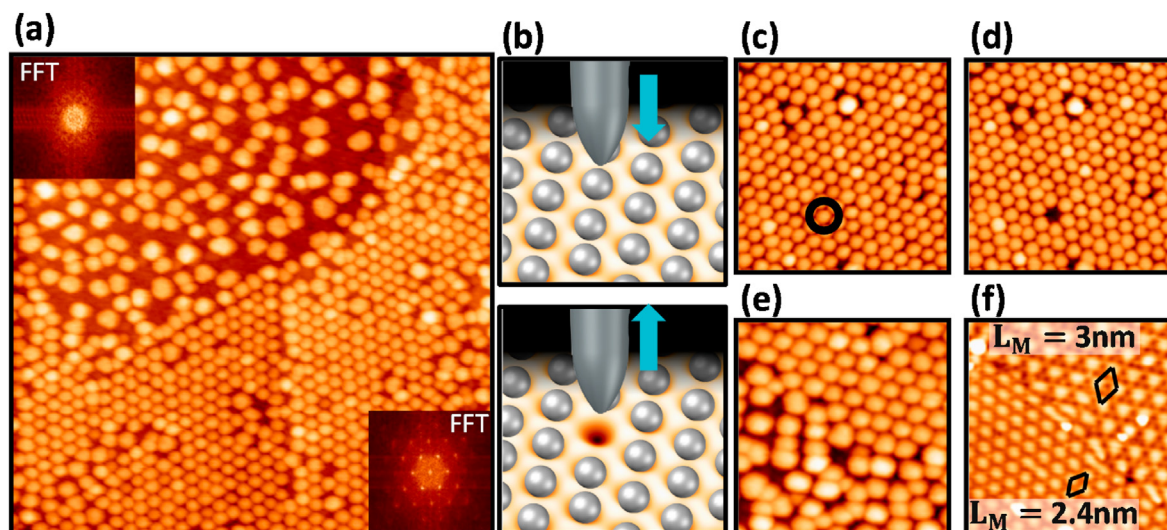


Fig. 1. Spatial distribution of Ir nanoparticles over the graphene/Rh(111) surface. a) Large scale STM image showing a high inhomogeneity in the size and the spatial distribution of the nanoparticles resulting after RT deposition of $0.50 \pm 0.05 \text{ ML}$ Ir. The insets show the Fast Fourier Transform of a zoomed-in region within the respective areas. b) Sketches of the procedure for removing nanoparticles. c)-d) STM topographies acquired on the same sample area prior and after the removal of the Ir nanoparticle encircled in black in (c). e)-f) STM images consecutively measured on the same sample area, close to a boundary between regions, where nanoparticles exhibit a different spatial distribution, before (e) and after (f) the removal of the Ir aggregates. The periodicity of the moiré in each region below the nanoparticles in e) is denoted in f) as L_M . Tunneling parameters: a) $V_s = +2.0 \text{ V}$, $I_T = 70 \text{ pA}$; size: $100 \times 100 \text{ nm}^2$; c)-d) $V_s = +2.0 \text{ V}$, $I_T = 70 \text{ pA}$; size: $40 \times 40 \text{ nm}^2$; e) $V_s = +2.0 \text{ V}$, $I_T = 70 \text{ pA}$; size: $30 \times 30 \text{ nm}^2$ and f) $V_s = +0.6 \text{ V}$, $I_T = 1.5 \text{ nA}$; size: $30 \times 30 \text{ nm}^2$. (A colour version of this figure can be viewed online.)

($\sqrt{91} \times \sqrt{91}$)-R27° supercell of graphene is coincident with a ($2\sqrt{19} \times 2\sqrt{19}$)-R23.4° of the Rh(111) support.

Fig. 1 demonstrates that the size and spatial distributions of the nanoparticles are influenced by the rotational domain of graphene on Rh(111). It seems that the $\text{RD0}_{11 \times 11}$ moiré pattern, which, as mentioned, results from a perfect alignment of the graphene lattice with respect to the underlying metal surface, acts as a good template for the formation of nanoparticle superlattices. Conversely, the other rotational variant observed in Fig. 1f is unable to be a suitable template for the growth of ordered Ir nanoparticle networks. Then, what are the key parameters determining the formation of such superlattices on the $\text{RD0}_{11 \times 11}$ moiré template?

To answer the above raised question, the adsorption configuration of the nanoparticles on the $\text{RD0}_{11 \times 11}$ moiré pattern, which, as above mentioned, is the predominant one in G/Rh(111) surfaces, has been investigated. First, the positioning of the Ir nanoparticles over the periodic superstructure, associated to this moiré pattern, has been analyzed by removing them from different areas and determining the positions of the atomic aggregates in the surroundings of the resulting vacancy islands. Fig. 2a shows, as an example, a STM image acquired in a region of G/Rh(111) after deposition of 0.50 ± 0.05 ML Ir, which leads to an average nanoparticle size of 60 ± 6 atoms as estimated from the coverage and by assuming that all moiré cells are filled. Nanoparticles have been partially removed using the STM tip following the procedure explained before. As a reference to determine the nanoparticle positioning, Fig. 2b displays an atomically resolved STM image of

the $\text{RD0}_{11 \times 11}$ moiré pattern, acquired within the region of Fig. 2a, in which the aggregates were previously removed. In agreement with previous literature [36,53], four subregions, where C atoms exhibit well-differenced chemical environments, can be distinguished inside the moiré supercell: top, hcp, fcc and bridge that are indicated by a circle, a triangle, a square and a star, respectively (see Fig. 2 c-f). Also, to allow a better interpretation of the STM topography displayed in Fig. 2a, a green lattice with the periodicity of the nanoparticle superlattice is overlaid on it, making easier the determination of the positioning of the atomic aggregates within the moiré cell. As observed, nanoparticles are preferentially centered on hcp regions (triangle), although sometimes they also can be found on fcc ones (square). A similar behavior has been found after Ir or other transition metals deposition on G/Ir(111) [6,30]. Furthermore, Ir or Pt nanoparticle superlattices have also been grown on G/Ru(0001), but in this substrate aggregates were found on fcc moiré subregions [34,54].

This spatial selectivity is related to the chemical reactivity modulation induced in the graphene layer by the metal surface. It has been reported that on strongly interacting graphene-metal interfaces, like G/Rh(111), those graphene areas within the moiré unit cell showing a strong hybridization with the metal surface display much larger reactivity than other less coupled areas, those more separated from the surface [37–40]. Notice that the hybridization degree is correlated with the local arrangement of carbon atoms with respect to the ones of the substrate underneath. Namely, the enhance of the reactivity is maximized in those moiré

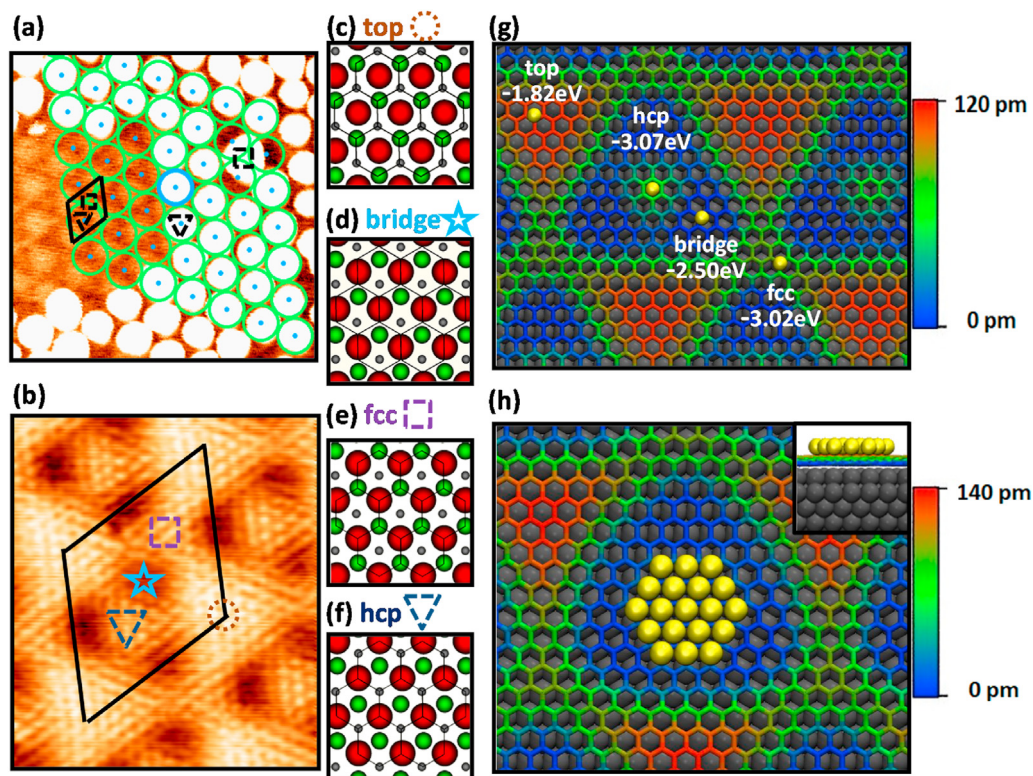


Fig. 2. Ir adsorption on the $\text{RD0}_{11 \times 11}$ moiré of the graphene/Rh(111) surface. a) Large scale STM image showing, simultaneously, both the nanoparticle network and the $\text{RD0}_{11 \times 11}$ moiré on a certain area (left of the image) after removal of the aggregates on top (image size: 25×25 nm²). b) Atomic resolution STM image acquired after nanoparticle removal on the uncovered region of (a). Top, bridge, fcc and hcp subregions are indicated by a brown circle, blue star, purple square and a dark blue triangle, respectively (image size: 5.6×6.4 nm²). c)-f) Schemes of the registry of C atoms of graphene with respect to the Rh atoms of the substrate within top, bridge, fcc and hcp subregions, respectively. Red, green and gray balls correspond to first, second and third layer of Rh respectively. g) Optimized geometry and its corresponding adsorption energy as obtained by DFT calculations for individual adatoms adsorbed within each of the four high symmetry subdivisions of the $\text{RD0}_{11 \times 11}$ moiré. The color bar indicates the relative heights of C atoms, choosing the closes C atom as a zero-reference. h) Optimized geometry of a nanoparticle comprising 19 Ir atoms on the hcp subregion of the $\text{RD0}_{11 \times 11}$ moiré pattern. The color bar indicates the relative heights of C atoms, choosing the closes C atom as a zero-reference. The inset shows a side view of the nanoparticle. Tunneling parameters: a) $I_T = 0.1$ nA; $V_S = +2.2$ V b) $I_T = 2.8$ nA; $V_S = +0.15$ V. (A colour version of this figure can be viewed online.)

areas where carbon atoms are located on top positions with respect to the metal ones, leaving their first neighbors carbon atoms on hollow positions [6,55]. This strong hybridization is the origin of the induced reactivity on the graphene, which also varies at the atomic scale: The high hybridization with the metal of the carbon atoms located on top positions destroys the G- π band, leading to the decoupling of their first neighbors, and giving rise to a local enhancement of the chemical reactivity. These atoms are even able to change its hybridization state to sp^3 upon adatom adsorption [37,55]. The adsorption of Ir nanoparticles follows, in this regard, a similar trend.

To obtain an accurate view of the bonding of Ir on the $RDO_{11 \times 11}$ moiré pattern, the adsorption of both individual adatoms and aggregates with sizes up to 19 atoms has been studied by DFT first-principles calculations as implemented in the VASP package [46], using plane waves with an energy cutoff of 400 eV, PBE + D2 [49,50] as exchange correlation functional and PAW [47,48] pseudopotentials (see Methods for more details). Fig. 2g schematically shows the relaxed geometry for the adsorption of an individual Ir adatom on each of the four different moiré subregions of the $RDO_{11 \times 11}$ moiré pattern. Most stable adsorption positions with respect to the graphene are different for each subregion: hollow for the hcp; top, on a carbon atom that has a metal atom below, for the fcc; and close to top for bridge and top subregions. This rich behavior has been reported for transition metal adsorbates on G/Ru(0001) [56] associated to a convolution between the electronic structure of the adatoms and the chemical reactivity at different areas that, as explained above, it is also modulated at the atomic scale for graphene on metals depending on the local arrangement of the carbon atoms with respect to the metal ones [37,55,56]. The adsorption energies for the optimized configurations shown in Fig. 2g on top, bridge, fcc and hcp subregions are, respectively: -1.82 , -2.50 , -3.02 , and -3.07 eV. Thus, within the $RDO_{11 \times 11}$ moiré pattern, hcp and fcc regions are clearly the most energetically favorable adsorption sites for the adsorption of individual Ir atoms, being the hcp region slightly more favorable. The top region is clearly the less favorable area, with a large energy penalization, up to 1.25 eV. A similar behavior was found for metal adsorbates on G/Ru(0001), but in this case, the fcc region being more favorable than the hcp, in agreement with the experimental information [34,54,56].

As previously discussed, the experiments show a strong dependence of the moiré pattern on the spatial distribution of the Ir nanoparticles grown on top. Fig. 1e–f revealed that while well-ordered nanoparticle superlattices are formed on the $RDO_{11 \times 11}$ moiré pattern, on others exhibiting a significantly smaller periodicity (2.4 nm), aggregates were found to be randomly distributed over the surface. Aimed to extract conclusions of the highest generality, a systematic investigation of the influence of the rotational domain on the spatial distribution of the atomic aggregates grown on top, has been performed. To this end, the above described methodology (removing nanoparticles from the G/Rh(111) surface) has been employed close to boundaries between regions of differently distributed Ir aggregates. Fig. 3a–f shows examples of the analysis of the spatial distribution of Ir nanoparticles close to boundaries between regions of the $RDO_{11 \times 11}$ moiré underneath ($L_M = 3$ nm), which are used as a reference, and one of the other rotational variants. The periodicity of the moiré pattern found after the removal of the nanoparticles in each region is indicated in the respective STM image (L_M). Thus, according to Fig. 3a–f, rotational domains resulting in moiré patterns with $L_M = 2.9$ and 2.8 nm lead to ordered networks, while other with smaller periodicities ($L_M = 2.4$, 2.2, 2.0 and 1.6 nm) display nanoparticles with a larger size and randomly scattered over the surface. Moreover, from Fig. 3a–f, it is also inferred that the density of nanoparticles is

smaller as the moiré periodicity decreases. To quantify this trend, from the STM data obtained in the present work, the average number of nanoparticles per moiré unit cell is plotted versus the underlying moiré periodicity in Fig. 3g. Data shown in Fig. 3g are divided into two groups according to the spatial distribution of the nanoparticles. Group I is associated to the formation of nanoparticle superlattices (including periodicities within the 2.8–3 nm range), while group II is associated to disordered spatial distributions of Ir. These disordered distributions appear when Ir adsorption takes place on moiré patterns with periodicities ranging from 1.6 to 2.6 nm. The STM analysis summarized in Fig. 3 demonstrates that, the G/Rh(111) interface is the first one reported to our best knowledge, in which there are several moiré patterns with different periodicities giving rise to the formation of metal nanoparticle superlattices. These observed variations in the superlattice periodicity, although narrow, could give rise to significantly modifications in the properties of the nanoparticle lattices.

To better understand the differences in the nanoparticle spatial distributions observed in Fig. 3, the adsorption of single adatoms has been studied, by DFT calculations, on a rotational domain with a moiré pattern of smaller periodicity. Specifically, calculations have been carried out for the rotational domain, on which the nanoparticles observed at the right part of Fig. 3f are formed. The moiré pattern associated to this rotational domain, hereinafter $RDO_{6 \times 6}$, has a periodicity of (6×6) with respect to the Rh(111) lattice and $(\sqrt{43} \times \sqrt{43}) - R7.6^\circ$ as referred to the atomic lattice of graphene [36]. Fig. 4a shows the optimized geometry of individual Ir adatoms on two different subregions of the moiré $RDO_{6 \times 6}$: “low” and “top”. Notice that, in this smaller moiré pattern, we could still distinguish between hcp and fcc regions but these areas are tiny, involving only ~ 4 C atoms only. In particular, we have calculated the adsorption on the hcp region. The corrugation between the lowest areas (hcp/fcc) and the highest (top) is 1.07 Å, slightly lower than in the larger moirés [36]. On the “low” subregion, according to the optimized geometry displayed in Fig. 4a, the Ir adatom is placed nearly over a C atom that is, in turn, located relatively close to a top position with respect to an underlying Rh atom. On the “top” moiré subdivision, the Ir adatom is placed nearly over a C atom. The adsorption energies for these two configurations on “top” and “low” subregions are -2.41 and -2.89 eV, respectively. For a better comparison, Table 1 collects these values together with the corresponding ones for the case of the $RDO_{11 \times 11}$ moiré pattern. According to these values, for the $RDO_{6 \times 6}$ moiré, the adsorption on the “low” subregion is favored with respect to that on the top sites. However, in this case, the energy difference between both configurations is less pronounced than in the case of the $RDO_{11 \times 11}$ moiré (0.48 eV vs. 1.25 eV). Also, it should be noted that the adsorption energy is higher on the hcp subregion of $RDO_{11 \times 11}$ than on the “low” one of the moiré $RDO_{6 \times 6}$. In spite of being an important feature, these energy differences do not constitute a suitable argument to entirely explain the absence of ordered lattices of nanoparticles in the smaller moiré patterns.

Another factor that could play a role in the cluster formation and the differences found with the moiré pattern size is the potential energy landscape of the diffusion processes for Ir adsorbates on the G/Rh(111). In particular, the interplay between the activation energies of these diffusion processes and the adsorption energy modulation exhibited along the moiré unit cell [57]. In order to shed light on this, possible diffusion paths of adatoms between different positions within the $RDO_{6 \times 6}$ moiré supercell have been calculated. It is worth noting that the large cell size prevents to carry out these calculations on the $RDO_{11 \times 11}$ moiré pattern, but large differences are not expected for the barriers as they are mainly determined by the local arrangement. Fig. 4b shows two

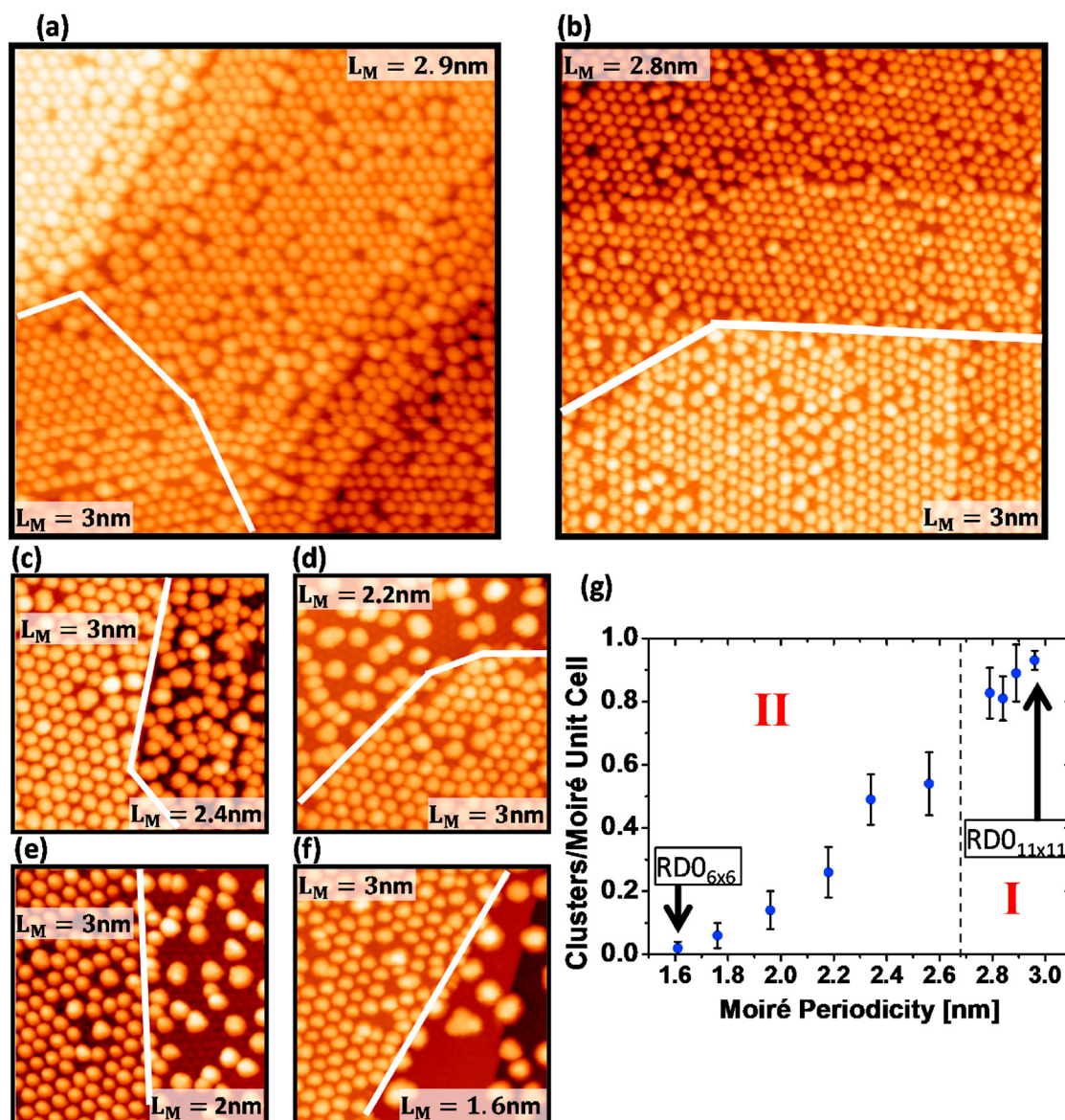


Fig. 3. Spatial distribution of Ir nanoparticles on different rotational variants of the graphene/Rh(111) surface. a)–f) Large scale STM images illustrating the differences in the spatial distribution of Ir nanoparticles between areas, where the RDO_{11×11} moiré is underlying, which is taken as a reference ($L_M = 3\text{ nm}$), and others with different moiré periodicities underneath (L_M). Size: a) and b) $100 \times 100\text{ nm}^2$; c)–f) $45 \times 45\text{ nm}^2$. g) Plot of the average number of clusters per moiré unit cell as a function of the periodicity of the underlying moiré pattern. Data are classified into two groups: Group I corresponds to moiré templates giving rise to ordered nanoparticle lattices; group II, associated to moiré patterns for which well-ordered arrays are not formed. Tunneling parameters: a) $V_s = -2.0\text{ V}$, $I_T = 0.2\text{ nA}$; b), c) and d) $V_s = +2.0\text{ V}$, $I_T = 70\text{ pA}$; e) $V_s = +2.2\text{ V}$, $I_T = 50\text{ pA}$; f) $V_s = +2.2\text{ V}$, $I_T = 30\text{ pA}$. (A colour version of this figure can be viewed online.)

different diffusion paths for individual Ir adatoms, initially placed on the configuration giving rise to the maximum adsorption energy (in the “low” subregion of the RDO_{6×6} moiré pattern). The obtained diffusion barriers are plotted in Fig. 4c and d and their maximum values are 0.41 eV and 0.52 eV for path I and II respectively. The values of these diffusion barriers show that, at RT, Ir individual atoms could travel across the whole moiré unit cell. The modulation in the adsorption energy, which is of a similar order than the diffusion barriers, would imply that, at that temperature, although top areas could be reached, the probability of finding Ir atoms in these areas would be significantly smaller. Paths between adjacent supercells can be found through non-unfavorable areas. The same mechanism works for the larger moirés, but there, as the reactivity difference is larger, accumulation of Ir atoms on either hcp or fcc subregions would be expected. However, considering the high

reactivity of Ir atoms, we cannot discard that the complex process of cluster formation involved small aggregates of two, three Ir atoms instead of isolate adatoms. The Potential Energy Surface (PES) sensed by these aggregates could be quantitatively different from the single adatom one, but we can assume that the modulation between favorable and non-favorable areas inside the moiré is also kept for them as it is directly based on the enhancement of the chemical reactivity of the graphene induced locally by the metal surface.

Attending to the above arguments, the richness of significantly different chemical environments for the C atoms seems to be a key factor for the formation of ordered networks in the G/Rh(111) interface. That is, remarkable differences in the adsorption energies between subregions while keeping similar energy barriers for the diffusion jumps. However, essentially these features are similar in

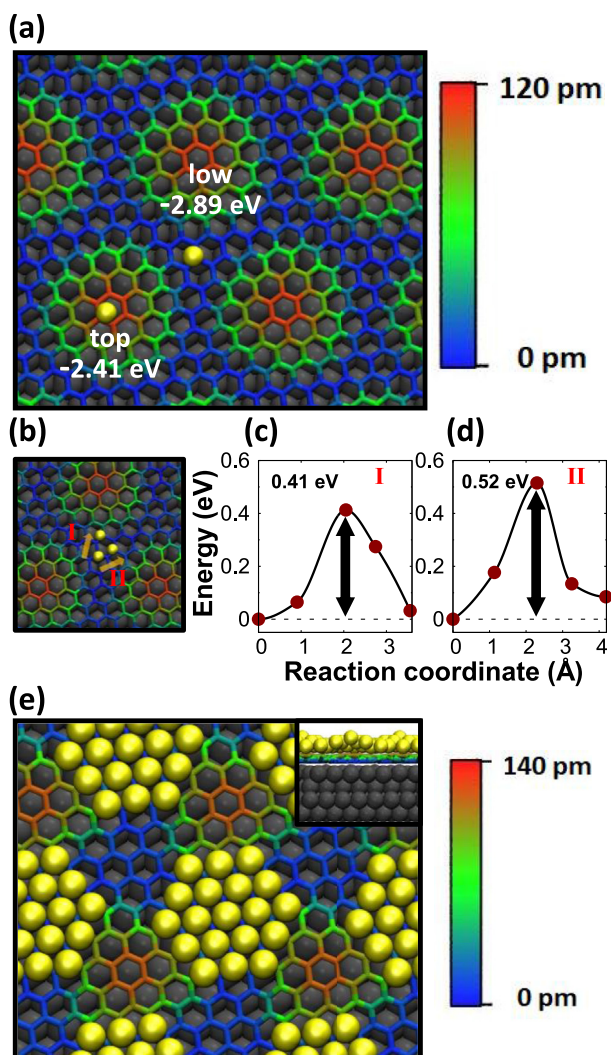


Fig. 4. Ir adsorption on the $\text{RD0}_{6 \times 6}$ moiré pattern. a) Optimized geometry and corresponding adsorption energy for individual Ir adsorbates on top and low subregions of the moiré pattern, which has a periodicity of (6×6) with respect to the Rh(111) lattice and $(\sqrt{43} \times \sqrt{43}) - R7.6^\circ$ as referred to the atomic lattice of graphene. b) Different diffusion paths, denoted as I and II, for an Ir adatom, initially placed on the energetically most favorable adsorption configuration within the low subregion. c)-d) Diffusion barriers obtained by CI-NEB calculations along these paths. e) Optimized geometry of nanoparticles comprising 19 Ir atoms on the low subregion of the $\text{RD0}_{6 \times 6}$ moiré pattern. The color bar indicates the relative heights of C atoms, choosing the closes C atom as a zero-reference. The inset shows a side view of the nanoparticle. (A colour version of this figure can be viewed online.)

Table 1

Adsorption energies of Ir adatoms on different subdivisions of the $\text{RD0}_{11 \times 11}$ and $\text{RD0}_{6 \times 6}$ moirés.

Moiré superstructure	Subregion	Adsorption energy [eV]
Moiré $\text{RD0}_{11 \times 11}$	top	-1.82
	bridge	-2.50
	fcc	-3.02
	hcp	-3.07
Moiré $\text{RD0}_{6 \times 6}$	“top”	-2.41
	“low”	-2.89

all moiré patterns with only a different degree of magnitude. Therefore, there should be something else playing an important role in the nanoparticle growth. The above analyses regarding the reactivity have been done on the basis of the adsorption of just a

single Ir, while, in reality, the formation of a nanoparticle involves several Ir atoms. Thus, DFT calculations for nanoparticle adsorption have been performed over the hcp subregion of the $\text{RD0}_{11 \times 11}$ moiré pattern, which is the preferred one according to STM images as that shown in Fig. 2a. Fig. 2h shows the optimized geometry of an atomic aggregate composed of 19 Ir atoms on the hcp subdivision of the $\text{RD0}_{11 \times 11}$ moiré pattern. Ir atoms are located on top of carbon atoms that are placed on hollow position with respect to the metal surface, the most reactive carbons of G/Rh(111). Thus, an isolate Ir atom prefers to adsorb on hollow position, in order to maximize the interaction of its reactive *d* orbitals with the three reactive carbon atoms on the hcp moiré region [55]. But upon cluster formation some of their states are used to interact with other Ir leaving only one state to form a bond with just one reactive C atom which changes its hybridization state to sp^3 , leading to an alternate bonding scheme on top of these more reactive C atoms. Notice that the cluster has spread out reaching some bridge subregions, as a consequence of the limited amount of available space on the preferential hcp subregion. A similar behavior has been observed in the adsorption of smaller 7-atoms Ir clusters. Although they are too small to be compared with experimentally observed nanoparticles (see further details and discussion in the supporting information), they can provide useful insights on the cluster formation. The large size of the combined cluster-moiré system prevents the possibility of performing a systematic study including larger Ir nanoparticles with different sizes and shapes. However, a calculation of the difference in adsorption energy between a 7-atoms Ir cluster on the hcp area and on the fcc area of the $\text{RD0}_{11 \times 11}$ already provides insight into the reason why clusters are mainly found in hcp regions, in spite of the “small” difference in the adsorption energy of individual Ir atoms on hcp and fcc areas. The cluster adsorption energy on the hcp region has been found 3.05 eV lower than on fcc, i.e. more favorable. From this value a difference of adsorption energy per atom of 0.43 eV is obtained, which is significantly larger than that found for an individual atom between hcp and fcc regions and explains the larger proportions of clusters in hcp regions.

Calculations of the 19 Ir nanoparticle on the $\text{RD0}_{6 \times 6}$ moiré pattern have been also carried out. The optimized geometry obtained is displayed observed in Fig. 4e (see further details in the supporting information). The potential energy hypersurface of this case is so complex that convergence has been achieved only at ~ 0.05 eV/Å forces. In any case, the Ir nanoparticle seems to adsorb on a similar position with respect to the graphene lattice, over the C atoms of one sublattice. However the Ir cluster is highly corrugated and C do not show the sp^3 hybridization. This corrugation is not found in the case of the $\text{RD0}_{11 \times 11}$ as can be observed by comparison of the insets in Figs. 2h and 4e which display a side view of the respective nanoparticles. It is clearly observed that the cluster has invaded the top subregions: there is not enough room in this moiré unit cell to accommodate an Ir cluster of this size on the more favorable adsorption areas. However, the occupancy of these unfavorable sites should not represent a significant energy penalty, given the rather limited differences in adsorption energy for individual Ir atoms on the different sites.

In summary, the combination of our results for the adsorption of single Ir atoms and Ir clusters on the two moirés illustrate the energy balance that controls the optimal cluster size: the competition between the internal Ir cluster energy (as a result of Ir–Ir interactions) and the Ir cluster-substrate energy. Strong Ir–Ir interactions would always favor aggregation, as observed in the large nanoparticles grown on smaller moiré patterns (e.g. $\text{RD0}_{6 \times 6}$). However, our calculations for the interaction of individual Ir atoms with the substrate support that, in the larger moirés, the growth of the metallic clusters should be limited by the significant differences in the Ir adsorption energies (more than 1.25 eV) across the

different moiré areas.

Since the size of the more favorable adsorption areas increases with the moiré periodicity, we should expect the formation of larger clusters. However, cluster growth will stop as soon as the highly unfavorable top areas have to be occupied. On the contrary, those energy differences are significantly reduced in the small moirés (below 0.5 eV), supporting a broad distribution of cluster sizes. Thus, in large enough rotational domains (for instance $\text{RDO}_{11 \times 11}$), the system maximizes its total energy with the formation of a homogeneous distribution of smaller clusters that fit precisely on the most favorable adsorption areas.

4. Conclusion

The formation of Ir nanoparticle superlattices on the G/Rh(111) surface has been studied by means of a combination of STM measurements and DFT calculations. The spatial distribution of the resulting nanoparticles after RT Ir deposition displays a great variability, including various ordered and highly monodisperse networks with different periodicities. Thus, the G/Rh(111) strongly interacting system is the first reported substrate to our best knowledge able to provide multiple templates to nanoparticle superlattices with different periodicities. This feature is possible thanks to the remarkable variations of the chemical reactivity along the moiré pattern unit cell and the presence of multiple rotational domains in this G-metal interface. Nanoparticles removal using the STM tip has allowed to uncover the surface underneath showing the inhomogeneity exhibited by the different moiré patterns found along graphene monolayers grown on Rh(111). While on moiré supercells with larger periodicities the nanoparticles formed on top are arranged into ordered networks, some other disordered arrangements have been also found on moiré patterns with a smaller unit cell size.

Aimed to understand the observed differences between larger and smaller sized moiré patterns, the adsorption of both individual Ir adatoms and planar Ir clusters (7 and 19 atoms) has been analyzed on the $\text{RDO}_{11 \times 11}$ moiré, which is the most common on the G/Rh(111) surface and the one with largest periodicity, and on the $\text{RDO}_{6 \times 6}$ one that is characterized by a much smaller periodicity. From this analysis, it can be deduced that nanoparticle superlattice formation is ruled by the combination of several factors. The existence of distinctive chemical environments throughout the moiré patterns unit cell, which are modulated by the G-metal interaction. The local arrangement of C atoms with respect to the metal atoms underneath, which determines the possibility to establish the required bonds in the aggregate formation, and the size of the most favorable adsorption areas of the unit cell, that controls the initial anchoring of the nanoparticles and may affect their final size. Our results point out that, only those moiré patterns above a certain size fulfill all the necessary requirements to allow the ordered growth of Ir nanoparticles. The findings presented here could be of interest for to further works on other interfaces comprising a 2D material layer and a metal substrate, paving the way for an improved control of the metal nanoparticle arrangements. The richness in nanoparticle spatial distributions presents the G/Rh(111) interface as a useful benchmark for investigating the properties of metal nanoparticles, a required step for the design of future nanocatalysts and nanodots.

CRediT authorship contribution statement

Mariano D. Jiménez-Sánchez: Investigation, Visualization. **Carlos Romero-Muñiz:** Investigation, Visualization. **Pablo Pou:** Conceptualization, Investigation. **Rubén Pérez:** Conceptualization, Supervision, Funding acquisition. **José M. Gómez-Rodríguez:** Conceptualization, Supervision, Funding acquisition.

Declaration of competing interest

The authors declare that they have no known competing financial interests or personal relationships that could have appeared to influence the work reported in this paper.

Acknowledgements

Financial support from AEI and FEDER under projects MAT2016-77852-C2-2-R and MAT2017-83273-R (AEI/FEDER, UE) and from Spanish Ministerio de Ciencia e Innovación, through the “María de Maeztu” Programme for Units of Excellence in R&D (grant No. CEX2018-000805-M) is gratefully acknowledged. C.R.M. acknowledges funding from the Spanish MICINN via the Juan de la Cierva-Formación program (ref. FJC2018-036832). Computational time provided by the Red Española de Supercomputación at the Marenostrum Supercomputer (BSC, Barcelona) is also acknowledged. We thank A.J. Martínez-Galera for fruitful discussions.

Appendix A. Supplementary data

Supplementary data to this article can be found online at <https://doi.org/10.1016/j.carbon.2020.11.086>.

References

- [1] J. Jeevanandam, A. Barhoum, Y.S. Chan, A. Dufresne, M.K. Danquah, Review on nanoparticles and nanostructured materials: history, sources, toxicity and regulations, *Beilstein J. Nanotechnol.* 9 (2018) 1050–1074.
- [2] W.J. Stark, P.R. Stoessel, W. Wohlleben, A. Hafner, Industrial applications of nanoparticles, *Chem. Soc. Rev.* 44 (2015) 5793–5805.
- [3] M.C. Daniel, D. Astruc, Gold nanoparticles: assembly, supramolecular chemistry, quantum-size-related properties, and applications toward biology, catalysis, and nanotechnology, *Chem. Rev.* 104 (2004) 293–346.
- [4] K.L. Kelly, E. Coronado, L.L. Zhao, G.C. Schatz, The optical properties of metal nanoparticles: the influence of size, shape, and dielectric environment, *J. Phys. Chem. B* 107 (2003) 668–677.
- [5] D. Astruc, F. Lu, J.R. Aranzas, Nanoparticles as recyclable catalysts: the frontier between homogeneous and heterogeneous catalysis, *Angew. Chem. Int. Ed.* 44 (2005) 7852–7872.
- [6] A.T. N'Diaye, S. Bleikamp, P.J. Feibelman, T. Michely, Two-dimensional Ir cluster lattice on a graphene moiré on Ir(111), *Phys. Rev. Lett.* 97 (2006), 215501.
- [7] M. Grzelczak, J. Vermant, E.M. Furst, L.M. Liz-Marzán, Directed self-assembly of nanoparticles, *ACS Nano* 4 (2010) 3591–3605.
- [8] M.A. Boles, M. Engel, D.V. Talapin, Self-assembly of colloidal nanocrystals: from intricate structures to functional materials, *Chem. Rev.* 116 (2016) 11220–11289.
- [9] M. Jamet, V. Dupuis, P. Mélinon, G. Guiraud, A. Pérez, W. Wernsdorfer, A. Traverse, B. Baguenard, Structure and magnetism of well defined cobalt nanoparticles embedded in a niobium matrix, *Phys. Rev. B* 62 (2000) 493–499.
- [10] C.L. Haynes, R.P. Van Duyne, Nanosphere lithography: a versatile nanofabrication tool for studies of size-dependent nanoparticle optics, *J. Phys. Chem. B* 105 (2001) 5599–5611.
- [11] R. Jin, The impacts of nanotechnology on catalysis by precious metal nanoparticles, *Nanotechnol. Rev.* 1 (2012) 31–56.
- [12] B. Roldan Cuenya, F. Behafarid, Nanocatalysis: size- and shape-dependent chemisorption and catalytic reactivity, *Surf. Sci. Rep.* 70 (2015) 135–187.
- [13] B. Wang, B. Yoon, M. König, Y. Fukamori, F. Esch, U. Heiz, U. Landman, Size-selected monodisperse nanoclusters on supported graphene: bonding, isomerism, and mobility, *Nano Lett.* 12 (2012) 5907–5912.
- [14] S. Linas, F. Jean, T. Zhou, C. Albin, G. Renaud, L. Bardotti, F. Tournus, Moiré induced organization of size-selected Pt clusters soft landed on epitaxial graphene, *Sci. Rep.* 5 (2015), 13053.
- [15] A. Grüneis, D.V. Vyalikh, Tunable hybridization between electronic states of graphene and a metal surface, *Phys. Rev. B* 77 (2008), 193401.
- [16] R. Larciprete, et al., Oxygen switching of the epitaxial graphene-metal interaction, *ACS Nano* 6 (2012) 9551–9558.
- [17] A.J. Martínez-Galera, U.A. Schroeder, F. Huttmann, W. Jolie, F. Craes, C. Busse, V. Caciuc, N. Atodiresei, S. Blügel, T. Michely, Oxygen orders differently under graphene: new superstructures on Ir(111), *Nanoscale* 8 (2016) 1932–1943.
- [18] F. Huttmann, A.J. Martínez-Galera, V. Caciuc, N. Atodiresei, S. Schumacher, S. Standop, I. Hamada, T.O. Wehling, S. Blügel, T. Michely, Tuning the van der Waals interaction of graphene with molecules via doping, *Phys. Rev. Lett.* 115 (2015), 236101.
- [19] S. Schumacher, et al., Europium underneath graphene on Ir(111):

- intercalation mechanism, magnetism, and band structure, *Phys. Rev. B* 90 (2014) 235437.
- [20] S. Schumacher, et al., The backside of graphene: manipulating adsorption by intercalation, *Nano Lett.* 13 (2013) 5013–5019.
- [21] S. Schumacher, D.F. Förster, M. Rösner, T.O. Wehling, T. Michely, Strain in epitaxial graphene visualized by intercalation, *Phys. Rev. Lett.* 110 (2013), 086111.
- [22] M. Petrović, et al., The mechanism of caesium intercalation of graphene, *Nat. Commun.* 4 (2013) 2772.
- [23] E. Grånäs, J. Knudsen, U.A. Schröder, T. Gerber, C. Busse, M.A. Arman, K. Schulte, J.N. Andersen, T. Michely, Oxygen intercalation under graphene on Ir(111): energetics, kinetics, and the role of graphene edges, *ACS Nano* 6 (2012) 9951–9963.
- [24] M. Papagno, S. Rusponi, P.M. Sheverdyaeva, S. Vlaic, M. Etzkorn, D. Pacilé, P. Moras, C. Carbone, H. Brune, Large band gap opening between graphene Dirac cones induced by Na adsorption onto an Ir superlattice, *ACS Nano* 6 (2012) 199–204.
- [25] S. Rusponi, M. Papagno, P. Moras, S. Vlaic, M. Etzkorn, P.M. Sheverdyaeva, D. Pacilé, H. Brune, C. Carbone, Highly anisotropic Dirac cones in epitaxial graphene modulated by an island superlattice, *Phys. Rev. Lett.* 105 (2010), 246803.
- [26] A.J. Martínez-Galera, J.M. Gómez-Rodríguez, Influence of metal support in-plane symmetry on the corrugation of hexagonal boron nitride and graphene monolayers, *Nano Res.* 11 (2018) 4643–4653.
- [27] M. Will, N. Atodiressei, V. Caciuc, P. Valerius, C. Herbig, T. Michely, A monolayer of hexagonal boron nitride on Ir(111) as a template for cluster superlattices, *ACS Nano* 12 (2018) 6871–6880.
- [28] A.J. Martínez-Galera, U.A. Schröder, C. Herbig, M.A. Arman, J. Knudsen, T. Michely, Preventing sintering of nanoclusters on graphene by radical adsorption, *Nanoscale* 9 (2017) 13618–13629.
- [29] C. Herbig, T. Knispel, S. Simon, U.A. Schröder, A.J. Martínez-Galera, M.A. Arman, C. Teichert, J. Knudsen, A.V. Krashenninikoy, T. Michely, From permeation to cluster Arrays: graphene on Ir(111) exposed to carbon vapor, *Nano Lett.* 17 (2017) 3105–3112.
- [30] A.T. N'Diaye, T. Gerber, C. Busse, J. Myslivecek, J. Coraux, T. Michely, A versatile fabrication method for cluster superlattices, *New J. Phys.* 11 (2009), 103045.
- [31] A.J. Martínez-Galera, I. Brihuega, J.M. Gómez-Rodríguez, Influence of the rotational domain in the growth of transition metal clusters on graphene, *J. Phys. Chem. C* 119 (2015) 3572–3578.
- [32] A.J. Martínez-Galera, I. Brihuega, A. Gutiérrez-Rubio, T. Stauber, J.M. Gómez-Rodríguez, Towards scalable nano-engineering of graphene, *Sci. Rep.* 4 (2014) 7314.
- [33] A.J. Martínez-Galera, J.M. Gómez-Rodríguez, Pseudo-ordered distribution of Ir nanocrystals on h-BN, *Nanoscale* 11 (2019) 2317–2325.
- [34] J. Díez-Albar, M.D. Jiménez-Sánchez, J.M. Gómez-Rodríguez, Nanowriting with clusters on graphene on Ru(0001), *J. Phys. Chem. C* 123 (2019) 5525–5530.
- [35] X.J. Liu, et al., Growth morphology and properties of metals on graphene, *Prog. Surf. Sci.* 90 (2015) 397–443.
- [36] A. Martín-Recio, C. Romero-Muñiz, A.J. Martínez-Galera, P. Pou, R. Pérez, J.M. Gómez-Rodríguez, Tug-of-War between corrugation and binding energy: revealing the formation of multiple moiré patterns on a strongly interacting graphene-metal system, *Nanoscale* 7 (2015) 11300–11309.
- [37] C. Romero-Muñiz, A. Martín-Recio, P. Pou, J.M. Gómez-Rodríguez, R. Pérez, Substrate-induced enhancement of the chemical reactivity in metal-supported graphene, *Phys. Chem. Chem. Phys.* 20 (2018) 19492–19499.
- [38] J.J. Navarro, et al., Organic covalent patterning of nanostructured graphene with selectivity at the atomic level, *Nano Lett.* 16 (2016) 355–361.
- [39] N. Guo, K.M. Yam, C. Zhang, Substrate engineering of graphene reactivity: towards high-performance graphene-based catalysts, *npj 2D Mater. Appl.* 2 (2018) 6.
- [40] M. Smerieri, E. Celasco, G. Carraro, A. Lusuan, J. Pal, G. Bracco, M. Rocca, L. Savio, L. Vattuone, Enhanced chemical reactivity of pristine graphene interacting strongly with a substrate: chemisorbed carbon monoxide on graphene/nickel(111), *ChemCatChem* 7 (2015) 2328–2331.
- [41] T. Reier, M. Oezaslan, P. Strasser, Electrocatalytic oxygen evolution reaction (OER) on Ru, Ir, and Pt catalysts: a comparative study of nanoparticles and bulk materials, *ACS Catal.* 2 (2012) 1765–1772.
- [42] F. Bizzotto, J. Quinson, A. Zana, J.J.K. Kirkensaard, A. Dworzak, M. Oezaslan, M. Arenz, Ir nanoparticles with ultrahigh dispersion as oxygen evolution reaction (OER) catalysts: synthesis and activity benchmarking, *Catal. Sci. Technol.* 9 (2019) 6345–6356.
- [43] Y. Sugita, T. Tamaki, H. Kuroki, T. Yamaguchi, Connected iridium nanoparticle catalysts coated onto silica with high density for oxygen evolution in polymer electrolyte water electrolysis, *Nanoscale Adv.* 2 (2020) 171–175.
- [44] O. Custance, S. Brochard, I. Brihuega, E. Artacho, J.M. Soler, A.M. Baró, J.M. Gómez-Rodríguez, Single adatom adsorption and diffusion on Si(111)-(7x7) surfaces: scanning tunneling microscopy and first-principles calculations, *Phys. Rev. B* 67 (2003), 235410.
- [45] I. Horcas, R. Fernández, J.M. Gómez-Rodríguez, J. Colchero, J. Gómez-Herrero, A.M. Baró, WSXM: a software for scanning probe microscopy and a tool for nanotechnology, *Rev. Sci. Instrum.* 78 (2007), 013705.
- [46] G. Kresse, J. Furthmüller, Efficient iterative schemes for ab initio total-energy calculations using a plane-wave basis set, *Phys. Rev. B* 54 (1996) 11169–11186.
- [47] P.E. Blöchl, Projector augmented-wave method, *Phys. Rev. B* 50 (1994) 17953–17979.
- [48] G. Kresse, D. Joubert, From ultrasoft pseudopotentials to the projector augmented-wave method, *Phys. Rev. B* 59 (1999) 1758–1775.
- [49] J.P. Perdew, K. Burke, M. Ernzerhof, Generalized gradient approximation made simple, *Phys. Rev. Lett.* 77 (1996) 3865–3868.
- [50] S. Grimme, Semiempirical GGA-type density functional constructed with a long-range dispersion correction, *J. Comput. Chem.* 27 (2006) 1787–1799.
- [51] H.J. Monkhorst, J.D. Pack, Special points for brillouin-zone integrations, *Phys. Rev. B* 13 (1976) 5188–5192.
- [52] G. Henkelman, H. Jónsson, Improved tangent estimate in the nudged elastic band method for finding minimum energy paths and saddle points, *J. Chem. Phys.* 113 (2000) 9978–9985.
- [53] E.N. Voloshina, Y.S. Dedkov, S. Torbrügge, A. Thissen, M. Fomin, Graphene on Rh(111): scanning tunneling and atomic force microscopy studies, *Appl. Phys. Lett.* 100 (2012), 241606.
- [54] K. Donner, P. Jakob, Structural properties and site specific interactions of Pt with the graphene/Ru(0001) moiré overlayer, *J. Chem. Phys.* 131 (2009), 164701.
- [55] P.J. Feibelman, Pinning of graphene to Ir(111) by flat Ir dots, *Phys. Rev. B* 77 (2008), 165419.
- [56] L.Z. Zhang, et al., Growth mechanism of metal clusters on a graphene/Ru(0001) template, *Adv. Mater. Interfaces* 1 (2014), 1300104.
- [57] O.V. Yazyev, A. Pasquarello, Metal adatoms on graphene and hexagonal boron nitride: towards rational design of self-assembly templates, *Phys. Rev. B* 82 (2010) 5.